Photochromism and Persistent Luminescence in Ni-Doped ZnGa(2)O(4)Transparent Glass-Ceramics: Toward Optical Memory Applications

Victor Castaing, Luidgi Giordano, Cyrille Richard, Didier Gourier, Mathieu Allix, Bruno Viana

DOI: 10.1002/ ((please add manuscript number))

Article type: Full Paper

Photochromism and persistent luminescence in Ni-doped $ZnGa_2O_4$ transparent glass-ceramics: toward optical memories applications

Victor Castaing, Luidgi Giordano†, Cyrille Richard, Didier Gourier, Mathieu Allix, Bruno Viana*

Dr. V. Castaing, L. Giordano, Prof. D. Gourier, Dr. B. Viana

Chimie-ParisTech, Institut de Recherche de Chimie Paris, PSL Research University, CNRS UMR8247, Paris, France

E-mail: castaing.victor@gmail.com

Dr. C. Richard

Université de Paris, CNRS, INSERM, UTCBS, Unité de Technologies Chimiques et Biologiques pour la Santé, Faculté de Pharmacie, 4 avenue de l'observatoire, 75006 Paris, France

Dr. M. Allix

CNRS, CEMHTI UPR3079, Université Orléans, F-45071 Orléans, France

Keywords: SWIR persistent luminescence, photochromism, $ZnGa_2O_4$, nano glass-ceramics, Nickel redox

ABSTRACT

Persistent luminescence and photochromism are two fascinating optical properties that involve charge trapping via defects and their release due to an external stimulation. In both processes, it is possible to define a "1" (or "on") and a "0" (or "off") optical state. Consequently, materials with one of these phenomena find major interest in view of designing smart, anticounterfeiting and optical information storage devices. Combining both processes within a single material can lead to a new generation of information storage phosphors, in which it may be possible to obtain three different optical states by playing on the external stimulations applied on the material. For that purpose, the elaboration of nickel-doped $ZnGa_2O_4$ spinel transparent nano glass-ceramics is presented in this work. The short-wave infrared (SWIR) emission, a broad band located at *ca.* 1275 nm, arises from Ni^{2+} cations located in gallium octahedral sites. SWIR persistent luminescence, arising from the same doping ion transition, can also be monitored after UV charging. Interestingly, UV irradiation

not only leads to persistent luminescence charging but also to reversible photochromism effect. By means of a complete optical characterization study combined to electron paramagnetic resonance measurements, the origins of both the persistent luminescence emission and the photochromism are explored. Finally, a discussion on the advantages of such material combining both persistent luminescence and photochromism properties, leading to three possible optical states of the material, is dressed in view of possible optical memory systems.

1.Introduction

Due to the increasing production and consumption of information, new innovative information storage materials are highly demanded. Amongst others, optical information storage materials take their advantages from their performances, *i.e.* their high storage capacity and exceptional rewritability, and their low ecological impact, as for example the low energy consumption during operation.[1–5] In these materials, an external optical stimulation is applied to the material to "write" the information. Then, another external stimulation, that can be thermal, electrical, mechanical, or optical, may be applied to the material to return to the initial optical state. Photochromic materials, which color can change while applying light irradiation, show increasing interests in that application fields. Indeed, in these materials, the information, that is the materials' color, can effectively be written optically and a thermal stimulation or another optical stimulation using another source can lead to a return to the original state.[6–8]

Persistent phosphors, that are able to emit light for a long time after excitation stoppage due to optimized optical energy storage by defects within the material, belongs to another materials family that recently found interest in view of developing anticounterfeiting[9–13] and optical information storage devices. [9,12,14–17] In that case, the information, which is the material emission with the charging source off, is stored with energetic sources (UV or blue) irradiation. The return to the original state can then be monitored optically, whereby it can be stimulated thermally (thermally stimulated luminescence, TSL) or optically (optically stimulated luminescence, OSL) using a lower energy source as a red or NIR LED. With visible persistent emission, a silicon-based detector or the human eye can read the optical information. However, due to the relatively low persistent emission it would be difficult for both the human eye and the silicon-based detector to read the information under day light or in an illuminated room. SWIR persistent luminescence takes their advantages in those

conditions. Indeed, as the illumination in rooms is now supplied by white LEDs with no contribution in the infrared range, it is possible to detect persistent luminescence in the SWIR range with an InGaAs-based detector in an w-LED illuminated room.

Within the last 25 years, persistent phosphors have been brought to the research forefront after two major discoveries, leading to a wide spectral range of afterglow emission. First, the discovery of $SrAl_2O_4:Eu^{2+},Dy^{3+}$ in 1996 has led to the extensive research of visible persistent phosphors with suitable morphologies for night signalization, night vision display without providing energy.[18–22] On the other hand, the elaboration of persistent phosphors targeting optical *in vivo* imaging widely revived the research in the field in the late 2000s.[23–30] In view of optical *in vivo* imaging applications, the probe material must emit in one of the three partially transparent biological windows (BW), *i.e.* BW-I (620 – 950 nm), BW-II (1000 – 1350 nm) and BW-III (1500 – 1800 nm), to be efficiently detected from outside the body.[31–35] Due to lower light diffusion and lower tissues autofluorescence, optical imaging using persistent phosphors with emission in the short wave infrared (SWIR) range, and therefore in the BW-II and BW-III, has gained more interests recently. Since 2014 and the elaboration of Nd^{3+}-doped Sr_2SnO_4 persistent phosphor, only few materials with persistent luminescence in one of this two spectral regions have been designed.[36] The most efficient ones being the $Y_3Al_2Ga_3O_{12}$ co-doped with Nd^{3+},Ce^{3+},Cr^{3+} or Ce^{3+},Er^{3+} for persistent emission in the BW-I and BW-II or BW-I and BW-III respectively.[37–40] Few other materials have been reported,[41–44] but most of them have been elaborated by high temperature solid state methods, giving access to high crystalline quality bulk materials with significantly higher persistent luminescence properties compared to nanoparticles that must be used for *in vivo* proof of concept. Regarding $ZnGa_2O_4$, reported as the most developed persistent luminescence material for *in vivo* imaging purposes, few recent works report strategies to shift the afterglow emission towards longer wavelengths range. For instance, the host matrix modification strategy, aiming at red shifting the $^4T_2 \rightarrow {}^4A_2$ emission or the co-doping strategy, to induce persistent energy transfer to an emitting ion in the SWIR range, have recently been explored.[45,46] Finally, a last strategy, the replacement of the red emitting Cr^{3+} ion by a SWIR emitting ion in the $ZnGa_2O_4$ matrix (for instance Co^{2+} or Ni^{2+}), has briefly been evocated.[47]

This last strategy was chosen in the present work, where the replacement of Cr^{3+} by Ni^{2+} in $ZnGa_2O_4:Cr^{3+}$ nanocrystals, is studied optically and is then discussed using both optical and magnetic characterizations. Less than ten years ago, a new elaboration strategy, using glass crystallisation synthesis, has shown great possibilities to prepare nanoscale

phosphors with intensive persistent luminescence properties, that is especially beneficial for persistent luminescence feasibility.[48] Indeed, since their first elaboration in 2014, $ZnGa_2O_4$-doped transparent nano glass-ceramics (nGC) have not only been used to demonstrate the importance of elaboration and morphological parameters on the persistent luminescence properties but also to further improve their afterglow features. This is for instance the case in Yb^{3+},Cr^{3+} co-doped $ZnGa_2O_4$ transparent nano glass ceramics in which the persistent luminescence spectra is enlarged towards the SWIR region.[46,49] Nickel has already been used as a dopant in glass-ceramics with similar host matrices compositions as the one studied for $ZnGa_2O_4$:Cr^{3+} nGC.[50,51] In these works, the Ni^{2+} cations (located in the Ga^{3+} octahedral site) emission, in the SWIR range suitable for optical fibre amplifier in the infrared range, is reported. Still, no afterglow properties in the SWIR range of Ni^{2+} in gallate materials have been reported yet.

In the information storage field, materials presenting both persistent luminescence and photochromism have already been studied due to their unprecedented properties for this potential application.[52–55] Still, the two phenomena have often been attributed to similar origins and no material showing both properties with three different optical information states has been designed yet. In this work, we aim at designing persistent luminescence gallate nGC with afterglow emission located in the SWIR range with an additional reversible photochromism. Due to its photoluminescence properties in this spectral range, divalent nickel appeared as a promising doping agent candidate in $ZnGa_2O_4$. To ensure the nanometric size and the crystalline quality of the crystals, the materials were elaborated following the nano glass-ceramics elaboration process. As targeted, SWIR persistent emission of the nGC can be observed, originating from the charge de-trapping towards $^3T_2$ divalent nickel excited state that is followed by its radiative relaxation towards $^4A_2$ ground state. On the other hand, UV excitation not only leads to persistent luminescence (Pers. Lum.) charging but also to an unprecedent thermally and optically reversible photochromism of the zinc gallates nGC. In the present case, the occurrence of both persistent luminescence and photochromism lead to a material showing three different information states, that may be of interest for further information storage devices development. Along this work, we intended to study and explain the origin of the two processes through optical and electron paramagnetic resonance (EPR) characterization. Finally, the three distinct optical information states are defined and discussed.

2.Experimental

2.1. Materials synthesis. The Ni^{2+}-doped $ZnGa_2O_4$ transparent phosphors were prepared following a glass crystallization method. Based on our previous works on Cr^{3+}-doped $ZnGa_2O_4$ nGC,[48,49] the parent glass composition 65 SiO_2 – 5 Na_2O – 17 ZnO – 23 Ga_2O_3 – 0.125 NiO has been chosen. SiO_2 (99.7 %, Strem Chemicals), $Na_2CO_3.10H_2O$ (99.999 %, Aldrich Chemistry), ZnO (99.999 %, Strem Chemicals), Ga_2O_3(99.998 %, Strem Chemicals) and NiO (99.99 %, Aldrich Chemistry) have been weighted in appropriate amounts, thoroughly mixed in an agate mortar with ethanol and decarbonated by overnight heating at 900 °C. The resulting powder has been melted at 1625 °C for 20 minutes under air and subsequently quenched by soaking the bottom of the platinum crucible in room temperature water. The materials have then been heated at 550 °C for one hour to remove stress in the glasses. Finally, partial crystallization of the resulting brownish transparent glasses has been performed by thermal treatment at 1000 °C for 12 minutes under air with 10 °C.min^{-1} heating rate. The resulting glass-ceramic materials appear transparent with a blue color (see insert of Figure 1).

2.2 Structural and optical Characterisations. In order to identify the crystalline phases of the obtained materials, X-ray powder diffraction (XRPD) data were recorded using a Bragg Brentano D8 Advance Bruker diffractometer (CuKα radiation) equipped with a LynxEye XE detector over the 10-95 ° (2θ) angular range with a 0.024 ° step size. The crystallite size of the glass-ceramic samples was determined *via* Rietveld refinement using a fundamental parameters approach available in the JANA2006 software.[56]

Transmission Electron Microscopy (TEM) was used to characterize the nanostructure of the glass-ceramic samples. High-resolution transmission electron microscopy (HRTEM) was performed on a JEOL ARM 200F (JEOL Ltd.) cold FEG operating at 200 kV and equipped with a double spherical corrector.

An InGaAs camera (PyLoN IR, Princeton Instruments) coupled to a NIR monochromator (300 grooves per mm, Acton Spectra Pro, Princeton Instruments) was used to record the luminescence in the SWIR range. For both steady state photoluminescence (PL), persistent luminescence (Pers. Lum.) as well as for thermally stimulated luminescence (TSL) measurements, a 365 nm LED (ThorLabs) was used as the excitation source. The same 365 nm LED was used to induce photochromism which was studied optically and magnetically. An intense Xe plasma lamp (EQ-99X LDLS, Energetiq Inc.) coupled to a monochromator

was used as the variable source for the excitation spectra. The TSL glow curves were recorded after 365 nm excitation for 5 minutes at 13 K. The low temperature was achieved using a closed-cycle He-flow cryostat (Sumitomo Cryogenics HC-4E). The heating ramp was set to a constant value of 10 $K.min^{-1}$ using a LakeShore temperature controller. The PL intensity profiles were recorded using the same 365 nm LED and a 625 nm LED, also provided by ThorLabs. This red LED was used to partially recover the initial blue tint of the glass-ceramics.

Photochromism was investigated by recording the optical absorption difference spectra of the nGCs before and after UV (365 nm) irradiation, using a Carry 5000i spectrophotometer.

Electron Paramagnetic Resonance (EPR) spectra were recorded by a Bruker ELEXSYS E500 working at X-band (≈ 9.4 GHz) using a Bruker 4122SHQE/0111 resonator. A resonator allowing optical irradiation has been used for measurement at room temperature with *in situ* UV excitation provided by the 365 nm LED. The low temperature measurements were achieved using a liquid Helium flow cryostat. In this case, the samples had been UV irradiated *ex situ*. The simulations of EPR spectra were performed using the EasySpin software.[57,58]

The persistent luminescence images of the materials in the short-wave infrared range were obtained using a photon counting device (Princeton, NIRvana 640 ST) after charging using a UV lamp.

3.Results and discussion

3.1. Crystal structure and phase identification. Figure 1 shows the XRPD pattern of the as-prepared Ni-doped nano glass-ceramics. In good agreement with previous works, the diffraction diagram is composed of a weak and broad signal located at *ca.* 20-25 ° and several diffraction peaks.[48] The broad signal can be assigned to the remaining silica glassy matrix. The Rietveld refinement demonstrates that the nGC elaboration methods solely lead to the crystallization of the $ZnGa_2O_4$ spinel phase in which Zn and Ga occupy almost exclusively (spinel inversion degree of around 0.03)[59] tetrahedral and octahedral sites respectively. The crystallites size determined using the Rietveld refinement is 18 ± 1 nm, in good agreement with previous results obtained on the Cr^{3+} doped $ZnGa_2O_4$ nGC.[46,48,49] Dark nanoparticles embedded in a bright SiO_2-rich glassy matrix can be observed in the TEM bright field micrograph presented in Figure 1 b). An average 23 ± 6 nm nanocrystal size can be measured, which is close to the crystallite size determined with XRD, confirming the low size dispersion

of the nanocrystals obtained using the nGC method. Finally, the higher magnification TEM micrograph (see Supporting Information Figure S1) indicates the high crystalline quality of the obtained nanospinels. As displayed in the inset of Figure 1, the obtained glass-ceramics are transparent with a bluish color. Their transparency is again in good agreement with the nanometric size of the spinel crystals, as reported in previous works.[48]

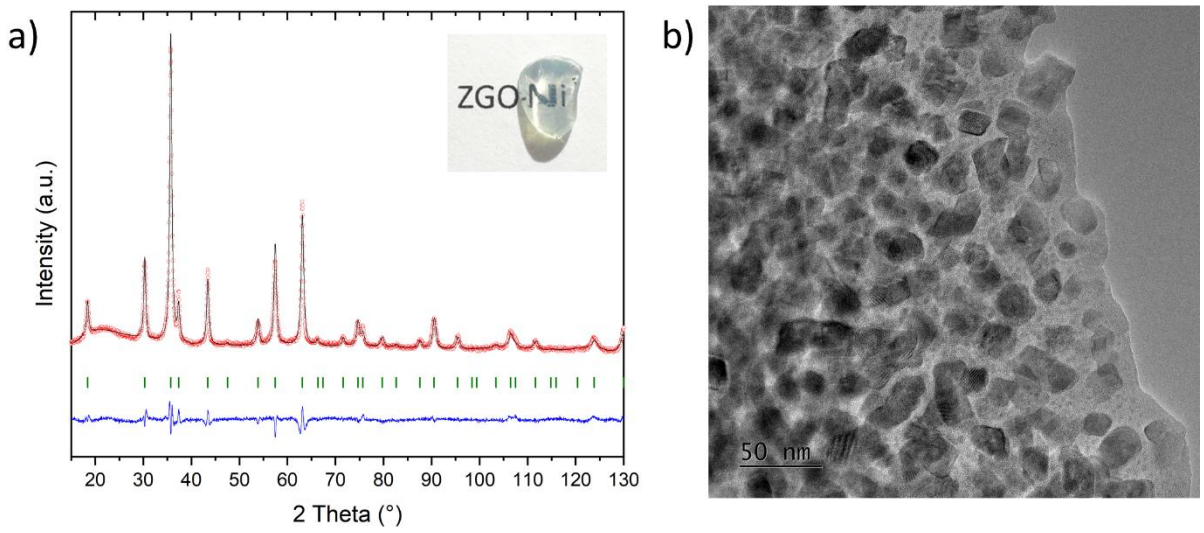

Figure 1. a) X-ray powder diffraction (XRPD) pattern of the Ni-doped $ZnGa_2O_4$ nGC synthesized by the melt quenching method followed by a second heat treatment stage (1000 °C for 12 min). The spinel zinc gallate diffraction peaks extracted from the ICCD database (01-071-0843) are presented in red. A photograph of the transparent nickel doped $ZnGa_2O_4$ nGC is displayed in insert. b) Bright field TEM micrograph of the Ni-doped $ZnGa_2O_4$ nGC.

3.2. SWIR photoluminescence properties of $ZnGa_2O_4:Ni^{2+}$ transparent glass ceramics.

As previously observed in other spinel structures, the Ni^{2+} doping ion is expected to substitute for gallium in octahedral sites due to its high crystal field stabilisation energy in octahedral symmetry.[60–62] Other valence states can be expected though, in particular Ni^{3+}. Figure 2 shows the PL spectra of nickel doped nGC under UV excitation (365 nm, 27397 cm^{-1}). The emission is composed of one broad band, with a full width at half maximum (FWHM) of *ca.* 180 nm, located at *ca.* 1275 nm (7843 cm^{-1}). This large emission band corresponds to the $^3T_2(F) \rightarrow {}^3A_2(F)$ transition of Ni^{2+}, indicating the incorporation of Ni^{2+} in the gallium octahedral site. The excitation spectrum of the SWIR emission in Ni-doped nGC is displayed in Figure 2 (b). It is composed of two bands located at *ca.* 250 nm and 360 nm, and a broad and composite band around 600 nm with a deep in its middle. The number and positions of excitation bands confirm that the emitting ion is Ni^{2+} located in gallium the octahedral sites.[50,51] Therefore, the excitation bands can be assigned as follows (Figure 2 (b)): the first

one can be attributed to the excitation through the host matrix band gap whereas the two others can be assigned to the Ni^{2+} transitions $^3A_2 \rightarrow {}^3T_1$ (^3P) and $^3A_2 \rightarrow {}^3T_1$ (^3F),^1E, respectively. The dip located at *ca.* 600 nm, and the related hump at *ca.* 620 nm, arise from a Fano effect that occurs when the $^3T_1$ (^3F) crosses the ^1E state. The degeneracy around the crossing point is lifted by the spin-orbit coupling, giving two states that can be described as mixtures of $^3T_1$ and ^1E states.[63] This interpretation is in agreement with the calculated crystal field parameters $D_q/B = 1.11$ using Underhill and Billing formula (see Supporting Information and Figure S2), which corresponds to the crossing of $^3T_1$ and ^1E states.[64] With lower intensity, the excitation through the spin-forbidden $^3A_2 \rightarrow {}^1T_2$ (^1D) nickel transition can also be observed at *ca.* 420 nm.

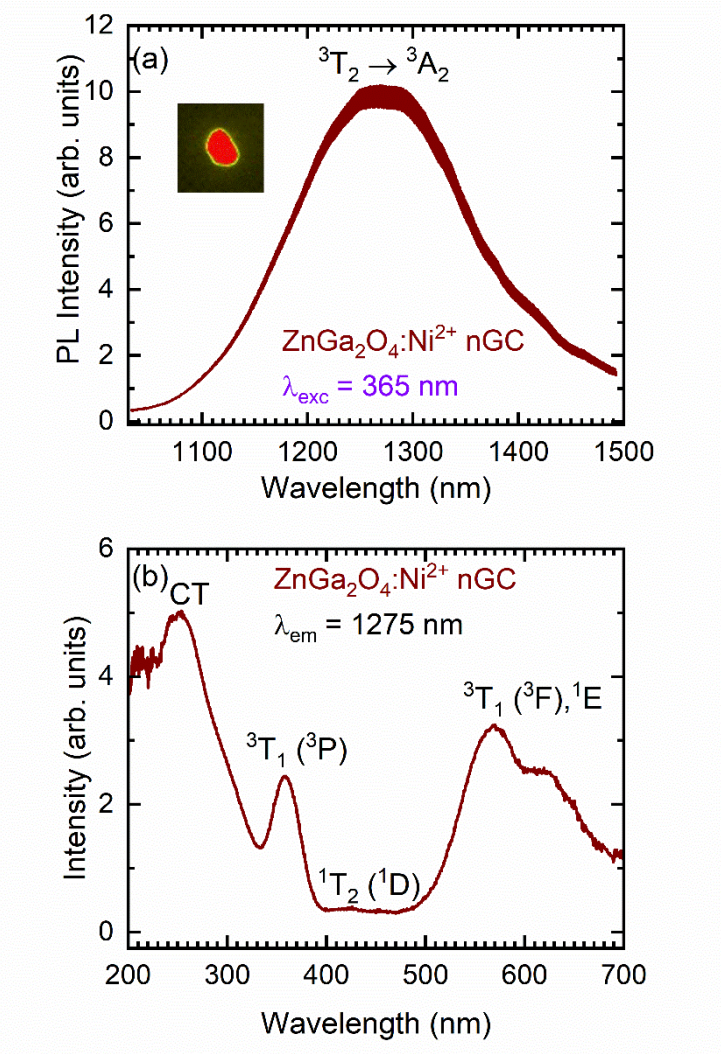

Figure 2. (a) Photoluminescence spectrum of the Ni-doped $ZnGa_2O_4$ nGC in the SWIR range under UV excitation (λ_{exc} = 365 nm). The inset shows a picture of the Ni-doped $ZnGa_2O_4$ nGC PL under the SWIR

camera. (b) Luminescence excitation spectrum of the same sample monitoring the $^3T_2 \rightarrow {}^3A_2$ emission in the SWIR range (λ_{em} = 1275 nm). PL and PLE spectra have been recorded at room temperature.

3.3. SWIR persistent luminescence properties. In the present work, Ni-doped $ZnGa_2O_4$ transparent nGCs have been prepared aiming at obtaining Ni^{2+} persistent luminescence (Pers. Lum.) in the SWIR range. Figure 3 (a) presents the SWIR Pers. Lum. decay of the materials. After charging for 5 minutes using a UV LED (λ_{exc} = 365 nm), Pers. Lum. can be recorded for more than five minutes using our detection set up. Moreover, as observed on the Pers. Lum. spectra, the persistent emission is, similarly to PL, located at *ca.* 1275 nm in the SWIR range. From the same shape observed for the Pers. Lum. and the PL spectra (see Figure 3 (b)), it can be deduced that the Pers. Lum. is also due to the Ni^{2+} $^3T_2$ (^3F) $\rightarrow$ $^3A_2$ (^3F) emission. Moreover, unlike its Cr^{3+}-doped counterpart, the Ni^{2+}-doped ZGO transparent nGC do not exhibit Pers. Lum. after red LED charging (λ_{exc} = 625 nm). Our previous results on the $ZnGa_2O_4$:Cr^{3+} transparent materials brought us to the hypothesis of a charge trapping at antisite defect pairs in the vicinity of the Cr^{3+} doping ion, which defect stability has been further confirmed by first principle calculations.[58,65,66] In this model, the electric field produced by the antisite defect pair on the Cr^{3+} doping ion could trigger the charge separation in the excited Cr^{3+} state and trapping while exciting with lower energy sources, such as red LEDs. In the present case, Ni^{2+} substitute for Ga^{3+}, creating a negatively charged Ni_{Ga}' defect. Consequently, the negatively charged antisite defects, *i.e.* Zn_{Ga}', should not be stable in the doping ion surrounding, so that the mechanism of charge generation and trapping should thus be different in the two compounds.

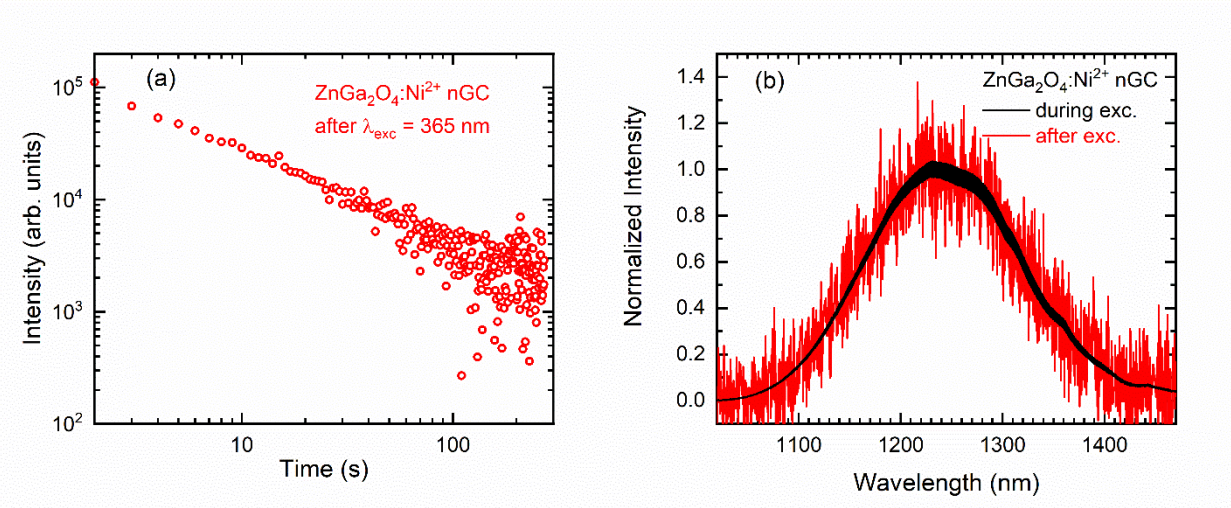

Figure 3. (a) Decay curve of Pers. Lum. in Ni-doped $ZnGa_2O_4$ nGC recorded after UV charging (λ_{exc} = 365 nm) for 5 min. (b) Persistent luminescence spectra of the same sample recorded 5 s after the UV excitation. For the sake of comparison, the photoluminescence spectra of the same sample just before excitation stoppage is presented in light red (λ_{exc} = 365 nm). The Pers. Lum. decay and spectrum have been recorded at room temperature.

In order to study the trap positions and to compare them to the ones of Cr^{3+}-doped $ZnGa_2O_4$ materials, thermoluminescence (TSL) measurements have been carried out. The TSL glow curve (Figure 4) shows a large band located at *ca.* 320 K and a very intense rise after 400 K. The latter corresponds to the infrared black body emission in this temperature range (the SWIR grating was centred at 1270 nm for this measurement). The weaker broad band centred at 320 K corresponds the signature of the charge release for the traps involved in the Pers. Lum. observed at RT. The glow peak maximum, slightly above RT, is of great interest for further applications. Even if it is difficult to establish comparison due to the weak signal-to-noise ratio, the position and shape of the TSL glow curve of the Ni^{2+}-doped $ZnGa_2O_4$ nGC seem quite similar to the Cr^{3+} doped ones. We may thus hypothesize that the SWIR persistent luminescence in these materials arise from charge trapping at antisite defects. In Cr^{3+}-doped zinc gallates, traps are related to antisite defects Ga_{Zn}° and Zn_{Ga}' and the charge separation is induced by the electric field at the neutral Ga_{Zn}°-Cr_{Cr}^{x}-Zn_{Ga}' clusters.[58,65,66] In Cr^{3+}-doped $ZnGa_2O_4$, the excitation of Cr^{3+} creates electron-hole pairs,[58,65] so that Cr^{3+} conserves its oxidation state during charging process, and the persistent luminescence intensity is limited by the number of available antisite defect pairs. However, here Ni^{2+} substitutes for Ga^{3+} in its octahedral site, thus forming a negatively charged defect Ni_{Ga}'. Positively charged defects, such as antisite defect Ga_{Zn}° or oxygen vacancy $V_O^{\circ\circ}$ can be created to compensate. In the present case of Ni^{2+} doping, formation of neutral Ga_{Zn}° – Ni_{Ga}'

pairs may be stabilized. The higher multiplicity of possibly stable defects in Ni^{2+}-doped $ZnGa_2O_4$ compared to its Cr^{3+} doped counterpart, may not only lead to the energy storage in Pers. Lum. efficient traps. Indeed, in the next section, charge trapping at deeper traps related to a materials photochromic effect is discussed.

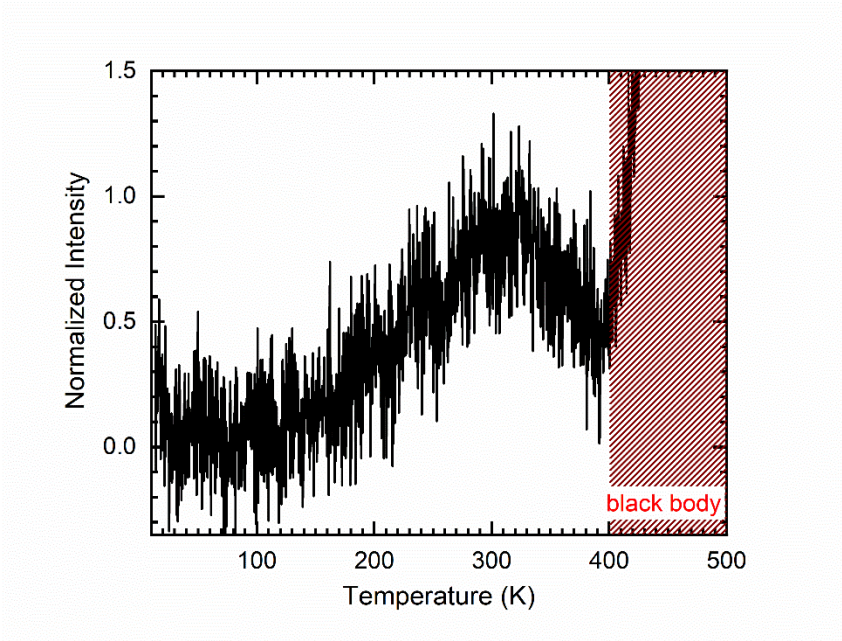

Figure 4. TSL profile of Ni-doped $ZnGa_2O_4$ nGC after UV lamp (λ_{exc} = 254 nm) charging at 15 K for 5 min.

3.4. Reversible photochromism. A worth mentioning observation was the color change of the transparent nGC after excitation in the UV range (365 nm). Indeed, as shown in Figure 5 (a), the blueish colour of the transparent nGC has turned to brownish yellow and remains stable after UV excitation stoppage. This photochromism is stable in time but is reversible using thermal treatment (T = 300 °C). Moreover, the color changes can be repeatedly obtained with UV excitation / thermal treatment cycles. The origin of this photochromism will be further discussed based on PL and EPR analyses. Finally, it is worth mentioning that this photochromism was not obtained with visible excitation sources.

The color change can be observed by representing the difference of absorbance spectra (noted Δ_{Abs}) after and before UV irradiation at 365 nm (Figure 5(b)). This difference spectrum shows a broad absorption tail in the UV/visible range (300 – 500 nm) with an apparent band peaking around 400 nm responsible for the color change of the transparent nGC. The shift of the absorption front towards the visible could be related to a partial photo-oxidation of Ni^{2+} into Ni^{3+} which, in the case of the presence of some Ni^{2+}-Ni^{2+} pairs, gives a small amount of

Ni^{2+}-Ni^{3+} pairs leading to intervalence charge transfer bands. Such bands are commonly observed for transition metal cations and are known to give some additional color.[67,68] The intensive absorption strength of such transitions, could explain the observed brownish/yellow color of the sample, even at very low doping contents. The band arising at around 475 nm (21053 cm^{-1}), evidenced by the second order derivative of Δ_{Abs} in Figure S3, could be due to the $^2E \rightarrow {}^2T_1, {}^2T_2$ transition of Ni^{3+} ($3d^7$) in low spin $t_2{}^5e$ configuration. This value is slightly larger than the value ~ 18 000 cm^{-1} measured for Ni^{3+} in $SrTiO_3$.[69]

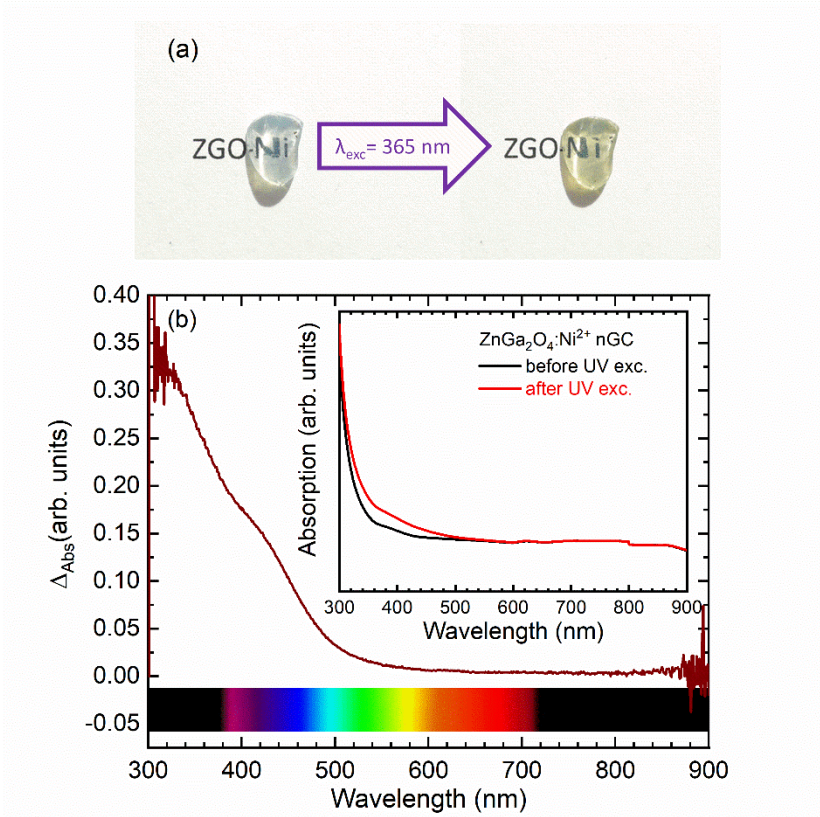

Figure 5. (a) Photographs of the Ni-doped $ZnGa_2O_4$ nGC sample before (left) and after (right) UV LED (λ_{exc} = 365 nm) irradiation. (b) Difference of absorption spectra after and before UV excitation (λ_{exc} = 365 nm). The absorption spectra, before (black) and after (red) UV excitation, are presented in insert. The absorption spectra have been recorded at room temperature.

This photochromism induces an increase of the material absorption in the UV / visible range, up to 500 nm. An evolution of the PL emission intensity can therefore be expected. Figure 6 (a) presents the evolution of the $^3T_2 \rightarrow {}^3A_2$ emission intensity of Ni^{2+} as a function of the UV excitation time. As soon as the excitation starts, an abrupt initial rise of the SWIR luminescence is observed. Then, the PL intensity appears to decrease gradually. After 15 minutes of excitation, a near-plateau stage is reached with a loss of about 42 % of the initial intensity. This decrease of the PL intensity is unexpected in persistent luminescence materials,

assuming a local trapping an detrapping model, in which a gradual increase of the PL emission with time is more likely to occur.[70,71] Thus, this decrease of PL intensity is possibly linked to the photochromism, that may hinder the photon absorption in the UV and thus, the emission. Also, a fraction of Ni^{2+} has been converted to Ni^{3+}, thus decreasing the Ni^{2+} emission intensity by the same amount. Moreover, it is worth noticing that this curve plotted in a log-log scale, starting when the excitation is stopped, gives the Pers. Lum. decay curve with 15 minutes excitation (Figure 3(a)). Comparing with the PL intensity, this demonstrates the relatively low persistent luminescence properties of the materials.

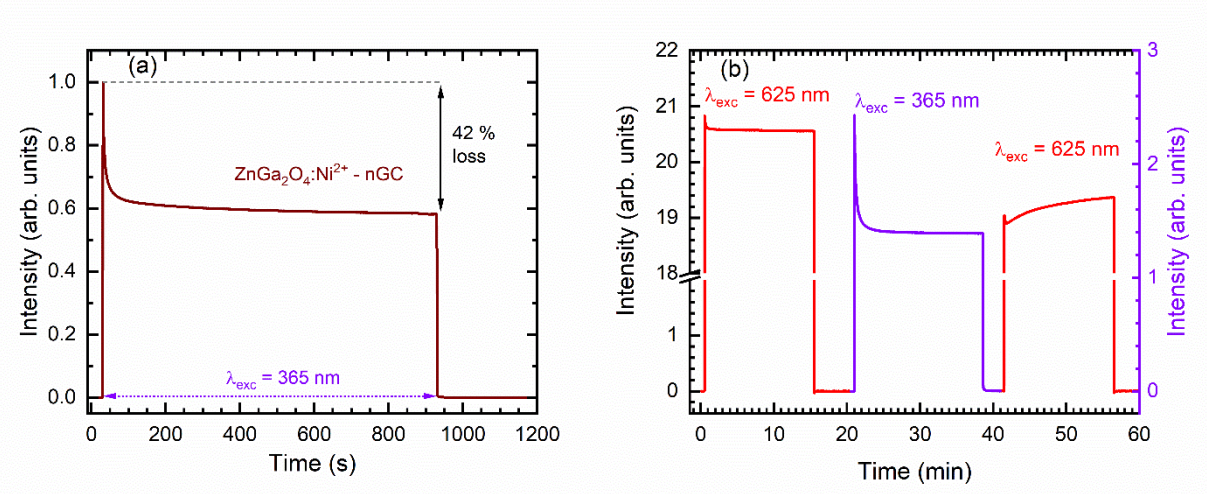

Figure 6. (a) Ni^{2+} $^3T_2 \rightarrow {}^4A_2$ photoluminescence intensity profile as a function of time (λ_{em} = 1275 nm). First, from 0 to 30 s no excitation was applied. Then, from 30 to 930 s, the sample was excited using a UV LED (λ_{exc} = 365 nm). Finally, from 930 to the end of the experiment, the UV excitation was stopped. (b) Ni-doped $ZnGa_2O_4$ nGC photoluminescence intensity profile as a function of time under two different irradiation wavelengths. First a red LED (λ_{exc} = 625 nm), then the UV LED (λ_{exc} = 365 nm) and finally the red LED (λ_{exc} = 625 nm) are used as the excitation sources. The PL profiles have been recorded at room temperature.

To learn more about the physical phenomena responsible of the photochromism, we investigated the effect of the excitation wavelength. In particular, a wavelength allowing direct excitation of d-d transition of Ni^{2+} but not energetic enough to pump in the charge transfer band was used in alternation with UV excitation. For that purpose, a 625 nm (E = 1.98 eV) LED has been used due to its ability to excite Ni^{2+} luminescence *via* the $^3A_2 \rightarrow {}^3T_2(^3F),{}^1E$ transition. The PL profile, displayed on Figure 6 (b), exhibits a very weak intensity decrease with the excitation time (*ca.* 1.3 % for 15 minutes of red LED illumination) compared to the same experiment using a UV LED. Moreover, the sample remains blue after that excitation. It appears that the excitation within the charge transfer band is required to

induce the photochromism. Subsequently, the material was excited by the 365 nm LED. On the related profile, the emission intensity decreases in time by about 42 % during UV irradiation. Finally, the brownish yellow photo-colored nGC was illuminated once again with the red LED to compare its PL intensity with the initial one (*i.e.* before the photochromism effect). The PL intensity excited at 625 nm recorded after UV irradiation is lower by about 9 % compared to the initial PL intensity. Interestingly, the PL intensity slowly increases with time. This could be due to optically induced release of electrons from deep trap and capture by Ni^{3+}, responsible from the increase of the 1275 nm emission of Ni^{2+}. However, on the absorption difference spectra (Figure 5 (b)), no clear defect absorption band could be observed around 365 nm. After longer illumination time (around one hour) with red light, the initial bluish color of the transparent nGC was retrieved. The possibility of optical bleaching of photochromism may be interesting in the field of optical memories as an information can be optically stored and read out.

3.5. Electron Paramagnetic Resonance study of the processes. EPR is a commonly used method to study the trapping centres in persistent luminescence materials.[58,72–75] In the case of Cr^{3+}-doped zinc gallates, no change of the EPR signal of Cr^{3+} has been observed upon charging the persistent luminescence with UV light, evidencing that no change of the oxidation state of Cr^{3+} occurs during charging and trapping.[58] The situation is different in Ni-doped nGCs, as shown in Figure 7. Before UV irradiation, the EPR spectrum shows only a signal in the 150 - 170 mT range, typical of Fe^{3+} impurities in solids. These impurities are probably located in the glassy matrix. As soon as the UV irradiation starts, an EPR signal appears at *ca.* 320 - 340 mT, corresponding to *g*-factors in the 2.3 to 2.1 range. After one minute of UV illumination, no EPR intensity change is observed. However, after stopping the excitation, the intensity of the UV-induced EPR signal remains unchanged, even 40 minutes after stopping the UV irradiation. Therefore, the new EPR signal cannot be related to the charge trapping/release involved in the Pers. Lum., as the latter decreases by more than one order of magnitude in 2 minutes. Heating the sample at 300 °C or exciting with red LED at 625 nm produces the total bleaching of the UV-induced EPR signal. Consequently, this EPR signal is connected to the photochromism and not to the Pers. Lum. properties of the nGC.

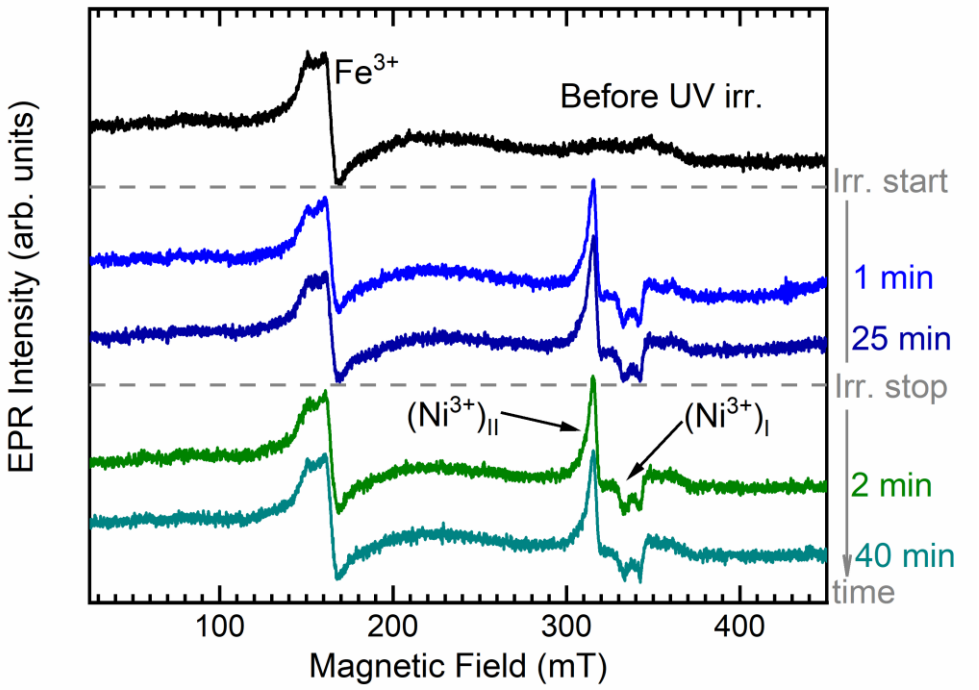

Figure 7. Room temperature X band EPR spectra of the Ni-doped $ZnGa_2O_4$ nGC before (black), during (blue) and after (green,) UV excitation (LED, λ_{exc} = 365 nm).

EPR signals with *g*-factors in the range 2.3 to 2.1 are typical for Ni^{2+} ($3d^8$) and Ni^{3+} ($3d^7$) in oxides.[76] Let us first consider Ni^{2+}, which corresponds to the normal state of nickel before UV irradiation. The ground state $^3A_2$ of Ni^{2+} in octahedral environment corresponds to a total spin $S = 1$, with three degenerated spin states $M_s = 0, \pm 1$. For an axial distortion of the octahedron, the S=1 state is split into a singlet $M_s = 0$ and and a doublet $M_s = \pm 1$ states by an amount $D \approx -4\lambda^2\delta/\Delta^2$, where Δ is the energy splitting between the $^3A_2$ and $^3T_2$ electronic states and δ the energy splitting of the $^3T_2$ state due to the axial distortion. This effect leaves the $M_s = 0$ state at lower energy than the $M_s \pm 1$ states. If the crystal field distortion is not too large, so that both M_s states 0 and $\pm$ 1 are thermally populated at room temperature, the resulting EPR signal of Ni^{2+} is a broad and isotropic line at g-factors given by $g_{//} \approx g_{\perp} \approx g_e - 8\lambda/\Delta$, where g_e =2.0023 is the free electron spin value. In a wide range of octahedral environments g varies from about 2.10 to 2.33.[76] In the particular case of a strong axial distortion such that $D >> kT$, only the $M_s = 0$ spin state is populated at room temperature, so that Ni^{2+} gives no EPR spectrum at X-band and at room temperature. The lack of EPR signal of Ni^{2+} in Ni-doped $ZnGa_2O_4$ may be explained by the presence of a strong axial distortion of

the octahedral crystal field of Ni^{2+}, which suggests that a large fraction of Ni^{2+} are in the form of the neutral Ni_{Ga}'-Ga_{Zn}° defect pairs proposed in previous sections, where the axial distortion is produced by the antisite defect Ga_{Zn}°. Also, as the EPR signal of Ni^{2+} is generally broad,[76] we cannot exclude that a fraction of Ni^{2+} is present in undistorted octahedral sites. In this case they may not be detected because of the corresponding low amplitude of the first derivative EPR signal (see below). Consequently, the EPR signal appearing upon UV irradiation and corresponding to the reversible photochromism is only due to Ni^{3+} ($3d^7$). Its shape is typical of a S=1/2 spin system, which implies that Ni^{3+} has the low spin configuration with a $^2E(t_2^6e)$ ground state. In the high-spin state $^4T_1(t_2^5e^2)$ the total spin is S = 3/2, which does not correspond to the experimental spectrum. The EPR signal of Ni^{3+} is composite with at least three components. In order to improve the signal-to-noise ratio, the EPR spectrum has been recorded at low temperature (5K) which allowed its simulation (Figure 8). The experimental spectrum can be fairly well reproduced by summing two components in the simulation. The first one is a symmetrical Lorentzian line with g = 2.21 whereas the second one is an anisotropic signal with $g_{\perp}$ = 2.28 and $g_{//}$ = 2.12. Thus the spectrum corresponds to two types of Ni^{3+}, referred to as $(Ni^{3+})_I$ and $(Ni^{3+})_{II}$, respectively, in a ratio of about 1:10. For a Ni^{3+} in octahedral environment with a ^2E ground state, the octahedron is axially distorted either by the Jahn-Teller effect or by a neighboring defect. The sequency of g-factor is $g_{//} > g_{\perp} > g_e$ for a compressed octahedron and $g_{\perp} > g_{//} > g_e$ for an elongated octahedron.[77] The g-factors measured for the $(Ni^{3+})_{II}$ centre clearly indicate an elongated octahedron, which is compatible with its attribution to a Ni_{Ga}^{x}-Ga_{Zn}° pair, whereby the positively charged antisite defect Ga_{Zn}° induces a decrease of the crystal field along the pair axis. The isotropic EPR line at g = 2.21 corresponding to the $(Ni^{3+})_I$ centre may be explained by a dynamical Jahn-Teller effect of $Ni^{3+}(^2E)$ in unperturbed octahedral site, which averages the anisotropy of the g-factor and gives $g_{av} = (g_{//} + 2g_{\perp})/3$. Taking the $g_{//}$ and $g_{\perp}$ values of $(Ni^{3+})_{II}$ centre, we obtain g_{av} = 2.22, which is close to the value g = 2.21 for $(Ni^{3+})_I$. Such dynamical Jahn-Teller effect has been observed in Ni^{3+}-doped $SrTiO_3$ and MgO for example.[77,78] Comparing these Ni^{3+} centres with Cr^{3+} in $ZnGa_2O_4$,[55] the $(Ni^{3+})_I$ and $(Ni^{3+})_{II}$ centres are the equivalent of Cr_{α} and Cr_{β}, respectively. In conclusion, the photochromism of Ni-doped $ZnGa_2O_4$ under UV irradiation may be attributed to hole trapping by Ni^{2+} ions. The presence of Ni^{3+} in undistorted octahedral site, namely $(Ni^{3+})_I$, implies that these Ni were in the 2+ state before hole trapping. The lack of observable EPR spectrum of Ni^{2+} in undistorted octahedral sites (*i.e* $(Ni^{2+})_I$) before UV irradiation is likely due to the important linewidth ΔB

of the EPR line of Ni^{2+},[76] which decreases the amplitude of the signal by a factor ~ ΔB^{-2}. In this case, the EPR line at g = 2.21 of $(Ni^{3+})_I$ is detectable because it has a smaller linewidth than its $(Ni^{2+})_I$ precursor.

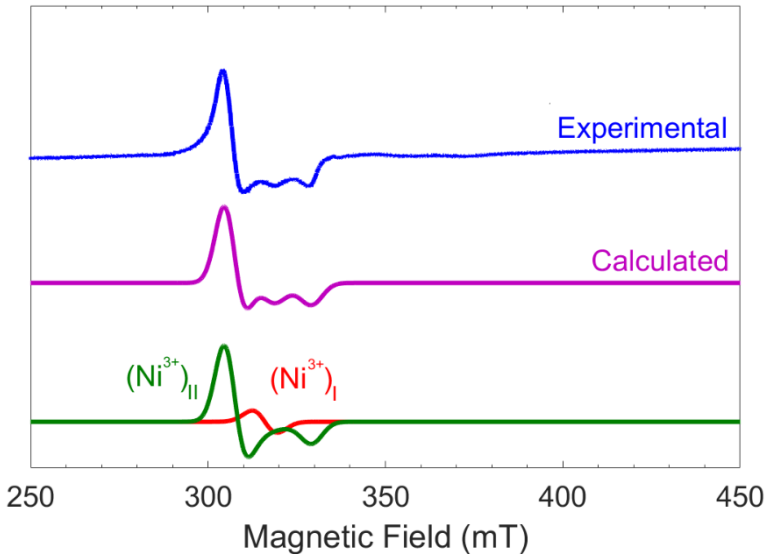

Figure 8. Low temperature (4K) X band EPR spectra of the Ni-doped $ZnGa_2O_4$ nGC after UV excitation λ_{exc} = 365 nm (blue). The simulation of the photogenerated Ni^{3+} signal is presented (violet) with the two component $(Ni^{3+})_I$ and $(Ni^{3+})_{II}$ (green and red respectively).

According to the present EPR and optical results, we may propose a mechanism explaining both the persistent luminescence and the photochromism. The first step is the creation of electron-hole pairs by the UV irradiation. Electrons and holes are trapped by shallow and deep trap levels. Shallow trap levels, which are responsible for the persistent luminescence, may be antisite defects Ga_{Zn}° and Zn_{Ga}', as in the case of Cr-doped $ZnGa_2O_4$,[65] according to the similitude of their TSL glow curves. The negatively charged Ni^{2+} (Ni_{Ga}') constitutes a deeper hole trap, as demonstrated by EPR (Ni^{3+} cations are stable at room temperature), and oxygen vacancies could act as deep electron trap levels. The effect of UV irradiation can be summarized by the following reactions (in Kröger-Vink notation):

hν (365 nm) → e' + h°

Deep trapping (photochromism):

$$Ni_{Ga}' + h^\circ \rightarrow Ni_{Ga}^{x} \quad i.e.\ (Ni^{3+})_I$$

$$Ni_{Ga}'\text{-}Ga_{Zn}^\circ + h^\circ \rightarrow Ni_{Ga}^{x}\text{-}Ga_{Zn}^\circ \quad i.e.\ (Ni^{3+})_{II}$$

$$V_O^{\circ\circ} \text{ (or } V_O^\circ) + e' \rightarrow V_O^\circ \text{ (or } V_O^{x})$$

Shallow trapping (persistent luminescence charging):

$$Zn_{Ga}' + h^{\circ} \rightarrow Zn_{Ga}^{x}$$

$$Ga_{Zn}^{\circ} + e' \rightarrow Ga_{Zn}^{x}$$

The persistent luminescence is due to thermal release of electrons and holes from shallow traps at room temperature followed by electron-hole (exciton) capture at Ni^{2+} site, giving an excited Ni^{2+}, noted $(Ni^{2+})^*$. This mechanism, which involves only the remaining Ni^{2+} and not Ni^{3+}, explains why the EPR intensity of Ni^{3+} is not modified during persistent luminescence:

$$e' + h^{\circ} + Ni^{2+} \rightarrow (Ni^{2+})^* \rightarrow Ni^{2+} + h\nu\ (1275\ nm)$$

The bleaching of photochromism is due to the release of electrons from deep traps by heating at high temperature or by illumination with red light, followed by recombination at $(Ni^{3+})_I$ and $(Ni^{3+})_{II}$ sites :

$$Ni_{Ga}^{x} + e' \rightarrow Ni_{Ga}'$$

$$Ni_{Ga}^{x}\text{-}Ga_{Zn}^{\circ} + e' \rightarrow Ni_{Ga}'\text{-}Ga_{Zn}^{\circ}$$

3.6. Towards optical memories applications. In this section we present an experimental description of the possible switching operations between optical states (see Figure 9 (a). Furthermore, from these experimental results, we could propose a schematic representation of the Ni redox in the different optical states as seen in Figure 9 (b).

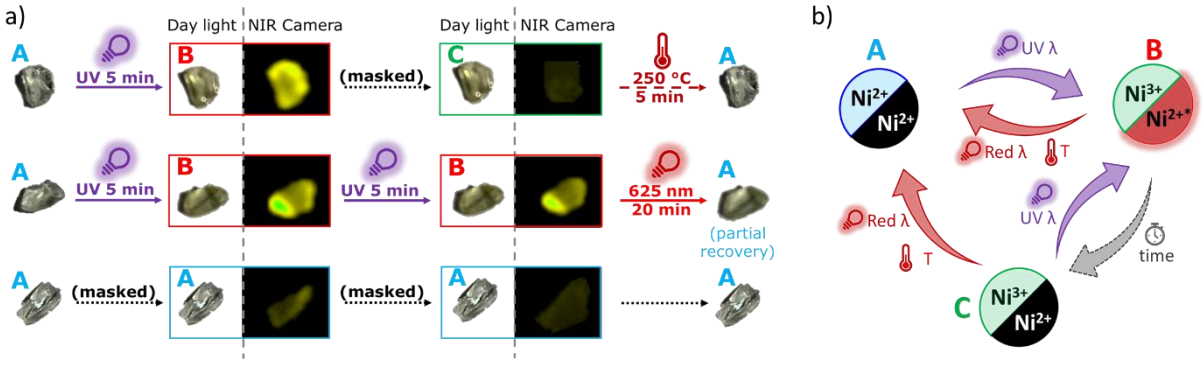

Figure 9. (a) Pictures of Ni-doped $ZnGa_2O_4$ nGC with different applied stimulations. The pictures with the white background are taken under day light whereas the ones with the black background are taken with the infrared imaging camera. (b) Schematized representation of the nickel ion behaviour under UV charging.

Before any excitation, the material is in its initial state, labelled as state A, as presented on Figure 9 (a). Here, the material is transparent with a blueish tint under day light, represented by the blue colour on the upper left part of state A in Figure 9 (b) and there is no afterglow emission in the dark, represented by the black color on the lower right part of state A (Figure 9 (b)). As shown by EPR, PL and TSL measurements, nickel in different oxidation states and different environments is responsible of both persistent luminescence and photochromism. Under UV irradiation, a part of Ni^{2+} ions (in pure and distorted octahedral environment) are converted to Ni^{3+} responsible of the photochromism, whereas the Ni^{2+} remaining unchanged after UV irradiation are involved in the Pers. Lum. Hereafter, the nGC are in the second optical state B *i.e.* the nGC are yellow-colored, the EPR signals of $(Ni^{3+})_I$ and $(Ni^{3+})_{II}$ are present, and there is SWIR persistent emission. Thermal release at room temperature from shallow traps is followed by electron-hole (exciton) capture by Ni^{2+}, leading to state C in Figure 9. This third optical state C is characterized by the brownish yellow color of the transparent nGC, the presence of the EPR signal, and the absence of SWIR Pers. Lum. State B can be restored back from state C by refilling the shallow traps through UV excitation. States B and C can be switched to the initial state A by electron release from deep traps, either by thermal treatment (*ca.* 300°C) or by red light excitation, followed by electron capture at Ni^{3+} sites (Figure 9).[…] As it has been demonstrated in the case of Cr-doped $ZnGa_2O_4$, and verified in this work by EPR, no change in the Ni^{3+} EPR intensity takes place during the persistent luminescence mechanism. For this reason, the persistent luminescence is only due to Ni^{2+} that have not been converted into Ni^{3+}, and the Pers. Lum. state is represented by Ni^{2+}*, an excited state of Ni^{2+} in state B (Figure 9 (b)). Figure 9 (b) schematizes the nickel cation memory effect under UV charging and the fading and recovery effects under temperature and lighting observed experimentally in Figure 9 (a). It is anticipated that these effects, leading to a material with the possibility of switching between three distinct optical states by means of optical and thermal stimulations, could open the path to storage and memory switch applications.

4. Conclusions. This work presents the elaboration and characterisation of $ZnGa_2O_4$:Ni^{2+} transparent nano glass-ceramics, while aiming at obtaining an optical information storage material with three different optical states based on persistent luminescence and photochromism. From the photoluminescence measurements, it appears that Ni^{2+} cations occupy Ga^{3+} octahedral sites. In addition to the observed photoluminescence, Ni^{2+} doping in the zinc gallate host leads to SWIR persistent luminescence after UV excitation. Still, the

persistent luminescence properties in this spectral region remains relatively weak, which can be explained by a small number of available trapped charge carriers, as demonstrated by the weak thermoluminescence signal. As in the case of Cr-doped $ZnGa_2O_4$ where no change of the oxidation state of Cr^{3+} is involved in the charging and the recombination, EPR shows that the persistent luminescence of Ni-doped $ZnGa_2O_4$ is controlled only by Ni^{2+} ions that have not been transformed into Ni^{3+} by the UV excitation. This might also explain why persistent luminescence is weak in this case. In addition to the SWIR emission, Ni^{2+} doping in $ZnGa_2O_4$ leads to an UV activated colour change of the material from blue to brownish yellow related to its partial photo-oxidation into Ni^{3+}, as demonstrated by the apparition of an UV-induced EPR signal stable at room temperature. This photochromism shows good reversibility either by thermal bleaching or, in a less efficient way, photo bleaching. Therefore, the studied materials show potential interests for anticounterfeiting applications as three different states can be easily obtained. Playing with light irradiation, temperature exposure or waiting times, appeared as an easy way to pass from an optical state to another one.

Present Addresses

[†]Department of Fundamental Chemistry, Institute of Chemistry, University of São Paulo, São Paulo-SP 05508-000, Brazil

Author Contributions

The manuscript was written through contributions of all authors. All authors have given approval to the final version of the manuscript.

ACKNOWLEDGMENTS

The authors thank Nadia Touati for her technical help with the EPR experiments. The authors acknowledge the French Research council for financial support within Paris Science et Lettres (PSL) and for funding the PERSIST project ANR-18-CE08-0012. L. Giordano wants to acknowledge the funds by the Coordenação de Aperfeiçoamento de Pessoal de Nível Superior – Brasil (CAPES) – CAPES 88887.371146/2019-00. This project is also co-funded by the European Union, the Region Centre Val de Loire, and the French minister of research (MESRI-DRRT). Europe is committed to the Centre-Val de Loire region with the European regional development fund (ERDF). This project has benefited from the facilities and expertise of the Platform MACLE-CVL.

Received: ((will be filled in by the editorial staff))
Revised: ((will be filled in by the editorial staff))
Published online: ((will be filled in by the editorial staff))

References

(1) Parthenopoulos, D. A.; Rentzepis, P. M. Three-Dimensional Optical Storage Memory. *Science* **1989**, *245* (4920), 843–845. https://doi.org/10.1126/science.245.4920.843.

(2) Day, D.; Gu, M.; Smallridge, A. Use of Two-Photon Excitation for Erasable–Rewritable Three-Dimensional Bit Optical Data Storage in a Photorefractive Polymer. *Opt. Lett.* **1999**, *24* (14), 948-950. https://doi.org/10.1364/OL.24.000948.

(3) Zhang, J.; Gecevičius, M.; Beresna, M.; Kazansky, P. G. Seemingly Unlimited Lifetime Data Storage in Nanostructured Glass. *Phys. Rev. Lett.* **2014**, *112* (3), 033901. https://doi.org/10.1103/PhysRevLett.112.033901.

(4) Gu, M.; Li, X.; Cao, Y. Optical Storage Arrays: A Perspective for Future Big Data Storage. *Light Sci. Appl.* **2014**, *3* (5), e177. https://doi.org/10.1038/lsa.2014.58.

(5) Gu, M.; Zhang, Q.; Lamon, S. Nanomaterials for Optical Data Storage. *Nat. Rev. Mater.* **2016**, *1* (12), 16070. https://doi.org/10.1038/natrevmats.2016.70.

(6) Wang, C.; Jin, Y.; Lv, Y.; Ju, G.; Chen, L.; Li, Z.; Duan, H.; Hu, Y. Reversible Luminescence Switching and Non-Destructive Optical Readout Behaviors of $Sr_3SnMO_7:Eu^{3+}$ (M = Sn, Si, Ge, Ti, Zr, and Hf) Driven by Photochromism and Tuned by Partial Cation Substitution. *Sens. Actuators B: Chem.* **2018**, *262*, 289–297. https://doi.org/10.1016/j.snb.2018.01.233.

(7) Sun, H.; Li, X.; Zhu, Y.; Wang, X.; Zhang, Q.; Hao, X. Achieving Multicolor Emission Readout and Tunable Photoswitching via Multiplexing of Dual Lanthanides in Ferroelectric Oxides. *J. Mater. Chem. C* **2019**, *7* (19), 5782–5791. https://doi.org/10.1039/C5TC02426A.

(8) Ren, Y.; Yang, Z.; Li, M.; Ruan, J.; Zhao, J.; Qiu, J.; Song, Z.; Zhou, D. Reversible Upconversion Luminescence Modification Based on Photochromism in $BaMgSiO_4:Yb^{3+},Tb^{3+}$ Ceramics for Anti-Counterfeiting Applications. *Adv. Optical Mater.* **2019**, *7* (15), 1900213. https://doi.org/10.1002/adom.201900213.

(9) Zhuang, Y.; Wang, L.; Lv, Y.; Zhou, T.-L.; Xie, R.-J. Optical Data Storage and Multicolor Emission Readout on Flexible Films Using Deep-Trap Persistent Luminescence Materials. *Adv. Funct. Mater.* **2018**, *28* (8), 1705769. https://doi.org/10.1002/adfm.201705769.

(10) Liu, J.; Zhuang, Y.; Wang, L.; Zhou, T.; Hirosaki, N.; Xie, R.-J. Achieving Multicolor Long-Lived Luminescence in Dye-Encapsulated Metal–Organic Frameworks and Its Application to Anticounterfeiting Stamps. *ACS Appl. Mater. Interfaces* **2018**, *10* (2), 1802–1809. https://doi.org/10.1021/acsami.7b13486.

(11) Yang, S.; Wu, D.; Gong, W.; Huang, Q.; Zhen, H.; Ling, Q.; Lin, Z. Highly Efficient Room-Temperature Phosphorescence and Afterglow Luminescence from Common Organic Fluorophores in 2D Hybrid Perovskites. *Chem. Sci.* **2018**, *9* (48), 8975–8981. https://doi.org/10.1039/C8SC03563F.

(12) Xu, J.; Tanabe, S. Persistent Luminescence Instead of Phosphorescence: History, Mechanism, and Perspective. *J. Lumin.* **2019**, 205, 581-620. https://doi.org/10.1016/j.jlumin.2018.09.047.

(13) Qian, J.; Zhao, Q.-Z. Anti-Counterfeiting Microstructures Induced by Ultrashort Laser Pulses. *Phys. Status Solidi A* **2020**, *217* (11), 1901052. https://doi.org/10.1002/pssa.201901052.

(14) Zhuang, Y.; Lv, Y.; Wang, L.; Chen, W.; Zhou, T.-L.; Takeda, T.; Hirosaki, N.; Xie, R.-J. Trap Depth Engineering of $SrSi_2O_2N_2:Ln^{2+},Ln^{3+}$ (Ln2+ = Yb, Eu; Ln3+ = Dy, Ho, Er) Persistent Luminescence Materials for Information Storage Applications. *ACS Appl. Mater. Interfaces* **2018**, *10* (2), 1854–1864. https://doi.org/10.1021/acsami.7b17271.

(15) Li, W.; Zhuang, Y.; Zheng, P.; Zhou, T.-L.; Xu, J.; Ueda, J.; Tanabe, S.; Wang, L.; Xie, R.-J. Tailoring Trap Depth and Emission Wavelength in $Y_3Al_{5-x}Ga_xO_{12}:Ce^{3+},V^{3+}$ Phosphor-in-Glass Films for Optical Information Storage. *ACS Appl. Mater. Interfaces* **2018**, *10* (32), 27150–27159. https://doi.org/10.1021/acsami.8b10713.

(16) Wang, C.; Jin, Y.; Lv, Y.; Ju, G.; Liu, D.; Chen, L.; Li, Z.; Hu, Y. Trap Distribution Tailoring Guided Design of Super-Long-Persistent Phosphor $Ba_2SiO_4:Eu^{2+},Ho^{3+}$ and Photostimulable Luminescence for Optical Information Storage. *J. Mater. Chem. C* **2018**, *6* (22), 6058–6067. https://doi.org/10.1039/C8TC01722K.

(17) Wang, B.; Li, X.; Chen, Y.; Chen, Y.; Zhou, J.; Zeng, Q. Long Persistent and Photo-stimulated Luminescence in Pr^{3+}-doped Layered Perovskite Phosphor for Optical Data Storage. *J. Am. Ceram. Soc.* **2018**, *101* (10), 4598–4607. https://doi.org/10.1111/jace.15703.
(18) Matsuzawa, T.; Aoki, Y.; Takeuchi, N.; Murayama, Y. A New Long Phosphorescent Phosphor with High Brightness, $SrAl_2O_4:Eu^{2+},Dy^{3+}$. *J. Electrochem. Soc.* **1996**, *143* (8), 2670–2673. https://doi.org/10.1149/1.1837067.
(19) Rojas-Hernandez, R. E.; Rubio-Marcos, F.; Rodriguez, M. Á.; Fernandez, J. F. Long Lasting Phosphors: $SrAl_2O_4$:Eu,Dy as the Most Studied Material. *Renew. Sustain. Energy Rev.* **2018**, *81*, 2759–2770. https://doi.org/10.1016/j.rser.2017.06.081.
(20) Van der Heggen, D.; Joos, J.; Rodríguez Burbano, D.; Capobianco, J.; Smet, P. Counting the Photons: Determining the Absolute Storage Capacity of Persistent Phosphors. *Materials* **2017**, *10* (8), 867. https://doi.org/10.3390/ma10080867.
(21) https://www.bbc.com/news/technology-27021291.
(22) https://www.huffpost.com/entry/glow-in-dark-bike-path-lane-sun-poland_n_57fd0732e4b068ecb5e1d57b.
(23) le Masne de Chermont, Q.; Chanéac, C.; Seguin, J.; Pellé, F.; Maîtrejean, S.; Jolivet, J.-P.; Gourier, D.; Bessodes, M.; Scherman, D. Nanoprobes with Near-Infrared Persistent Luminescence for in Vivo Imaging. *Proc. Natl. Acad. Sci. U. S. A.* **2007**, *104* (22), 9266. https://doi.org/10.1073/pnas.0702427104.
(24) Maldiney, T.; Lecointre, A.; Viana, B.; Bessière, A.; Bessodes, M.; Gourier, D.; Richard, C.; Scherman, D. Controlling Electron Trap Depth To Enhance Optical Properties of Persistent Luminescence Nanoparticles for In Vivo Imaging. *J. Am. Chem. Soc.* **2011**, *133* (30), 11810–11815. https://doi.org/10.1021/ja204504w.
(25) Maldiney, T.; Bessière, A.; Seguin, J.; Teston, E.; Sharma, S. K.; Viana, B.; Bos, A. J. J.; Dorenbos, P.; Bessodes, M.; Gourier, *et al*. The in Vivo Activation of Persistent Nanophosphors for Optical Imaging of Vascularization, Tumours and Grafted Cells. *Nat. Mater.* **2014**, *13* (4), 418–426. https://doi.org/10.1038/nmat3908.
(26) Van den Eeckhout, K.; Poelman, D.; Smet, P. Persistent Luminescence in Non-Eu^{2+}-Doped Compounds: A Review. *Materials* **2013**, *6* (7), 2789–2818. https://doi.org/10.3390/ma6072789.
(27) Viana, B.; Sharma, S. K.; Gourier, D.; Maldiney, T.; Teston, E.; Scherman, D.; Richard, C. Long Term in Vivo Imaging with Cr^{3+} Doped Spinel Nanoparticles Exhibiting Persistent Luminescence. *J. Lumin.* **2016**, *170*, 879–887. https://doi.org/10.1016/j.jlumin.2015.09.014.
(28) Liu, J.; Lécuyer, T.; Seguin, J.; Mignet, N.; Scherman, D.; Viana, B.; Richard, C. Imaging and Therapeutic Applications of Persistent Luminescence Nanomaterials. *Adv. Drug Deliv. Rev.* **2019**, *138*, 193-210. https://doi.org/10.1016/j.addr.2018.10.015.
(29) Viana, B.; Richard, C.; Castaing, V.; Glais, E.; Pellerin, M.; Liu, J.; Chanéac, C. NIR-Persistent Luminescence Nanoparticles for Bioimaging, Principle and Perspectives. **2020**, 163–197. In: Benayas, A., Hemmer, E., Hong, G., Jaque, D., (eds) Near Infrared-Emitting Nanoparticles for Biomedical Applications. *Springer,* Cham. https://doi.org/10.1007/978-3-030-32036-2_8.
(30) Fritzen, D. L.; Giordano, L.; Rodrigues, L. C. V. Opportunities for Persistent Luminescent Nanoparticles in Luminescence Imaging of Biological Systems and Photodynamic Therapy. *Nanomaterials* **2020**, *10* (10), 2015. https://doi.org/10.3390/nano10102015.
(31) Anderson, R. R.; Parrish, J. A. The Optics of Human Skin. *Journal of Investigative Dermatology* **1981**, *77* (1), 13–19. https://doi.org/10.1111/1523-1747.ep12479191.
(32) Weissleder, R. A Clearer Vision for in Vivo Imaging. *Nat. Biotechnol.* **2001**, *19* (4), 316–317. https://doi.org/10.1038/86684.
(33) Smith, A. M.; Mancini, M. C.; Nie, S. Second Window for in Vivo Imaging: Bioimaging. *Nat. Nanotechnol.* **2009**, *4* (11), 710–711. https://doi.org/10.1038/nnano.2009.326.
(34) Law, G.-L.; Wong, K.-L.; Lau, K.-K.; Lap, S.; Tanner, P. A.; Kuo, F.; Wong, W.-T. Nonlinear Optical Activity in Dipolar Organic–Lanthanide Complexes. *J. Mater. Chem.* **2010**, *20* (20), 4074. https://doi.org/10.1039/b926376d.

(35) Lo, W.-S.; Kwok, W.-M.; Law, G.-L.; Yeung, C.-T.; Chan, C. T.-L.; Yeung, H.-L.; Kong, H.-K.; Chen, C.-H.; Murphy, M. B.; Wong, K.-L.; *et al*. Impressive Europium Red Emission Induced by Two-Photon Excitation for Biological Applications. *Inorg. Chem.* **2011**, *50* (12), 5309–5311. https://doi.org/10.1021/ic102465j.

(36) Kamimura, S.; Xu, C.-N.; Yamada, H.; Terasaki, N.; Fujihala, M. Long-Persistent Luminescence in the near-Infrared from Nd^{3+}-Doped Sr_2SnO_4 for in Vivo Optical Imaging. *Jpn. J. Appl. Phys.* **2014**, *53* (9), 092403. https://doi.org/10.7567/JJAP.53.092403.

(37) Xu, J.; Tanabe, S.; Sontakke, A. D.; Ueda, J. Near-Infrared Multi-Wavelengths Long Persistent Luminescence of Nd^{3+} Ion through Persistent Energy Transfer in Ce^{3+},Cr^{3+} Co-Doped $Y_3Al_2Ga_3O_{12}$ for the First and Second Bio-Imaging Windows. *Appl. Phys. Lett.* **2015**, *107* (8), 081903. https://doi.org/10.1063/1.4929495.

(38) Xu, J.; Murata, D.; Ueda, J.; Tanabe, S. Near-Infrared Long Persistent Luminescence of Er^{3+} in Garnet for the Third Bio-Imaging Window. *J. Mater. Chem. C* **2016**, *4* (47), 11096–11103. https://doi.org/10.1039/C6TC04027F.

(39) Xu, J.; Murata, D.; Katayama, Y.; Ueda, J.; Tanabe, S. Cr^{3+}/Er^{3+} Co-Doped $LaAlO_3$ Perovskite Phosphor: A near-Infrared Persistent Luminescence Probe Covering the First and Third Biological Windows. *J. Mater. Chem. B* **2017**, *5* (31), 6385–6393. https://doi.org/10.1039/C7TB01332A.

(40) Xu, J.; Murata, D.; Ueda, J.; Viana, B.; Tanabe, S. Toward Rechargeable Persistent Luminescence for the First and Third Biological Windows via Persistent Energy Transfer and Electron Trap Redistribution. *Inorg. Chem.* **2018**, *57* (9), 5194–5203. https://doi.org/10.1021/acs.inorgchem.8b00218.

(41) Liang, Y.-J.; Liu, F.; Chen, Y.-F.; Wang, X.-J.; Sun, K.-N.; Pan, Z. New Function of the Yb^{3+} Ion as an Efficient Emitter of Persistent Luminescence in the Short-Wave Infrared. *Light Sci. Appl.* **2016**, *5* (7), e16124. https://doi.org/10.1038/lsa.2016.124.

(42) Liu, F.; Liang, Y.; Chen, Y.; Pan, Z. Divalent Nickel-Activated Gallate-Based Persistent Phosphors in the Short-Wave Infrared. *Adv. Opt. Mater.* **2016**, *4* (4), 562–566. https://doi.org/10.1002/adom.201500656.

(43) Kamimura, S.; Xu, C.-N.; Yamada, H.; Marriott, G.; Hyodo, K.; Ohno, T. Near-Infrared Luminescence from Double-Perovskite $Sr_3Sn_2O_7$:Nd^{3+}: A New Class of Probe for in Vivo Imaging in the Second Optical Window of Biological Tissue. *J. Ceram. Soc. Jpn.* **2017**, *125* (7), 591–595. https://doi.org/10.2109/jcersj2.17051.

(44) Nie, J.; Li, Y.; Liu, S.; Chen, Q.; Xu, Q.; Qiu, J. Tunable Long Persistent Luminescence in the Second Near-Infrared Window via Crystal Field Control. *Sci. Rep.* **2017**, *7* (1), 12392. https://doi.org/10.1038/s41598-017-12591-1.

(45) Pan, Z.; Castaing, V.; Yan, L.; Zhang, L.; Zhang, C.; Shao, K.; Zheng, Y.; Duan, C.; Liu, J.; Richard, C.; Viana, B. Facilitating Low-Energy Activation in the Near-Infrared Persistent Luminescent Phosphor $Zn_{1+x}Ga_{2-x}Sn_xO_4$:Cr^{3+} via Crystal Field Strength Modulations. *J. Phys. Chem. C* **2020**, *124* (15), 8347–8358. https://doi.org/10.1021/acs.jpcc.0c01951.

(46) Castaing, V.; Sontakke, A. D.; Xu, J.; Fernandez-Carrion, A. J.; Genevois, C.; Tanabe, S.; Allix, M.; Viana, B. Persistent Energy Transfer in ZGO:Cr^{3+},Yb^{3+} a New Strategy to Design Nano Glass-Ceramics Featuring Deep Red and Near Infrared Persistent Luminescence. *Phys. Chem. Chem. Phys.* **2019**, 21 (35), 19458–19468. https://doi.org/10.1039/C9CP02927C.

(47) Pellerin, M.; Chanéac, C.; Castaing, V.; Viana, B.; Gourier, D. Persistent Luminescence of Transition Metal (Co, Ni...)-Doped $ZnGa_2O_4$ Phosphors for Applications in the near-Infrared Range. In *Oxide-based Materials and Devices IX*; Teherani, F. H., Look, D. C., Rogers, D. J., Eds.; SPIE: San Francisco, United States, **2018**; p 65. https://doi.org/10.1117/12.2294986.

(48) Chenu, S.; Véron, E.; Genevois, C.; Garcia, A.; Matzen, G.; Allix, M. Long-Lasting Luminescent $ZnGa_2O_4$:Cr^{3+} Transparent Glass-Ceramics. *J. Mater. Chem. C* **2014**, *2* (46), 10002–10010. https://doi.org/10.1039/C4TC02081B.

(49) Castaing, V.; Sontakke, A. D.; Fernandez-Carrion, A. J.; Touati, N.; Binet, L.; Allix, M.; Gourier, D.; Viana, B. Persistent Luminescence of $ZnGa_2O_4$:Cr^{3+} Transparent Glass Ceramics: Effects of

Excitation Wavelength and Excitation Power. *Eur. J. Inorg. Chem.* **2017**, (44), 5114–5120. https://doi.org/10.1002/ejic.201700841.

(50) Gao, Z.; Liu, Y.; Ren, J.; Fang, Z.; Lu, X.; Lewis, E.; Farrell, G.; Yang, J.; Wang, P. Selective Doping of Ni^{2+} in Highly Transparent Glass-Ceramics Containing Nano-Spinels $ZnGa_2O_4$ and $Zn_{1+x}Ga_{2-2x}Ge_xO_4$ for Broadband near-Infrared Fiber Amplifiers. *Sci. Rep.* **2017**, *7* (1), 1783. https://doi.org/10.1038/s41598-017-01676-6.

(51) Zhang, Y.; Li, X.; Lai, Z.; Zhang, R.; Lewis, E.; Azmi, A. I.; Gao, Z.; Lu, X.; Chu, Y.; Liu, Y.; *et al.* Largest Enhancement of Broadband Near-Infrared Emission of Ni^{2+} in Transparent Nano-Glass Ceramics: Using Nd^{3+} as Sensitizer and Yb^{3+} as Energy Transfer Bridge. *J. Phys. Chem. C* **2019**, 123 (15), 10021-10027. https://doi.org/10.1021/acs.jpcc.9b00359

(52) Ueda, J.; Shinoda, T.; Tanabe, S. Photochromism and Near-Infrared Persistent Luminescence in Eu^{2+}-Nd^{3+}-Co-Doped $CaAl_2O_4$ Ceramics. *Opt. Mater. Express* **2013**, *3* (6), 787. https://doi.org/10.1364/OME.3.000787.

(53) Jin, Y.; Hu, Y.; Yuan, L.; Chen, L.; Wu, H.; Ju, G.; Duan, H.; Mu, Z. Multifunctional Near-Infrared Emitting Cr^{3+}-Doped $Mg_4Ga_8Ge_2O_{20}$ Particles with Long Persistent, Photostimulated Persistent Luminescence and Photochromism Properties. *J. Mater. Chem. C* **2016**, *4* (27), 6614-6625. https://doi.org/10.1039/C6TC01640E.

(54) Asami, K.; Ueda, J.; Tanabe, S. Long Persistent Luminescence and Blue Photochromism in Eu^{2+}-Dy^{3+} Co-Doped Barium Silicate Glass Ceramic Phosphor. *J. Lumin.* **2019**, *207*, 246–250. https://doi.org/10.1016/j.jlumin.2018.11.006.

(55) Yuan, L.; Jin, Y.; Zhu, D.; Mou, Z.; Xie, G.; Hu, Y. Ni^{2+}-Doped Yttrium Aluminum Gallium Garnet Phosphors: Bandgap Engineering for Broad-Band Wavelength-Tunable Shortwave-Infrared Long-Persistent Luminescence and Photochromism. *ACS Sustainable Chem. Eng.* **2020**, *8* (16), 6543–6550. https://doi.org/10.1021/acssuschemeng.0c01377.

(56) Petříček, V.; Dušek, M.; Palatinus, L. Crystallographic Computing System JANA2006: General Features. *Z. Kristallogr. Cryst. Mater.* **2014**, *229* (5). https://doi.org/10.1515/zkri-2014-1737.

(57) Stoll, S.; Schweiger, A. EasySpin, a Comprehensive Software Package for Spectral Simulation and Analysis in EPR. *J. Magn. Reson.* **2006**, *178* (1), 42–55. https://doi.org/10.1016/j.jmr.2005.08.013.

(58) Gourier, D.; Bessière, A.; Sharma, Suchinder. K.; Binet, L.; Viana, B.; Basavaraju, N.; Priolkar, K. R. Origin of the Visible Light Induced Persistent Luminescence of Cr^{3+}-Doped Zinc Gallate. *J. Phys. Chem. Solids* **2014**, *75* (7), 826–837. https://doi.org/10.1016/j.jpcs.2014.03.005.

(59) Allix, M.; Chenu, S.; Véron, E.; Poumeyrol, T.; Kouadri-Boudjelthia, E. A.; Alahraché, S.; Porcher, F.; Massiot, D.; Fayon, F. Considerable Improvement of Long-Persistent Luminescence in Germanium and Tin Substituted $ZnGa_2O_4$. *Chem. Mater.* **2013**, *25* (9), 1600–1606. https://doi.org/10.1021/cm304101n.

(60) Donegan, J. F.; Bergin, F. J.; Glynn, T. J.; Imbusch, G. F.; Remeika, J. P. The Optical Spectroscopy of $LiGa_5O_8$:Ni^{2+}. *J. Lumin.* **1986**, *35* (1), 57–63. https://doi.org/10.1016/0022-2313(86)90008-6.

(61) Suzuki, T.; Senthil Murugan, G.; Ohishi, Y. Spectroscopic Properties of a Novel Near-Infrared Tunable Laser Material. *J. Lumin.* **2005**, *113* (3–4), 265–270. https://doi.org/10.1016/j.jlumin.2004.10.022.

(62) Dugué, A.; Cormier, L.; Dargaud, O.; Galoisy, L.; Calas, G. Evolution of the Ni^{2+} Environment During the Formation of a MgO-Al_2O_3-SiO_2 Glass-Ceramic: A Combined XRD and Diffuse Reflectance Spectroscopy Approach. *J. Am. Ceram. Soc.* **2012**, *95* (11), 3483–3489. https://doi.org/10.1111/j.1551-2916.2012.05421.x.

(63) Taktak, O.; Souissi, H.; Souha, K. Electronic Structure and Fano Antiresonance of Chromium Cr(III) Ions in Alkali Silicate Glasses. *J. Lumin.* **2015**, *161*, 368–373. https://doi.org/10.1016/j.jlumin.2015.01.047.

(64) Underhill, A. E.; Billing, D. E. Calculations of the Racah Parameter B for Nickel (II) and Cobalt (II) Compounds. *Nature* **1966**, *210* (5038), 834–835. https://doi.org/10.1038/210834a0.

(65) Bessière, A.; Sharma, S. K.; Basavaraju, N.; Priolkar, K. R.; Binet, L.; Viana, B.; Bos, A. J. J.; Maldiney, T.; Richard, C.; Scherman, D.; *et al*. Storage of Visible Light for Long-Lasting

Phosphorescence in Chromium-Doped Zinc Gallate. *Chem. Mater.* **2014**, *26* (3), 1365–1373. https://doi.org/10.1021/cm403050q.

(66) De Vos, A.; Lejaeghere, K.; Vanpoucke, D. E. P.; Joos, J. J.; Smet, P. F.; Hemelsoet, K. First-Principles Study of Antisite Defect Configurations in $ZnGa_2O_4$:Cr Persistent Phosphors. *Inorg. Chem.* **2016**, *55* (5), 2402–2412. https://doi.org/10.1021/acs.inorgchem.5b02805.

(67) Martinat, B.; Gourier, D.; Lejus, A. M.; Vivien, D. Optical Properties of $LaMgAl_{11}O_{19}:Ti^{3+}$, a Potential Tunable Laser Material. *J. Solid State Chem.* **1990**, *89* (1), 147-154. https://doi.org/10.1016/0022-4596(90)90305-H.

(68) Taran, M. N.; Parisi, F.; Lenaz, D.; Vishnevskyy, A. A. Synthetic and Natural Chromium-Bearing Spinels: An Optical Spectroscopy Study. *Phys. Chem. Minerals* **2014**, *41* (8), 593–602. https://doi.org/10.1007/s00269-014-0672-2.

(69) Müller, K. A.; Berlinger, W.; Rubins, R. S. Observation of Two Charged States of a Nickel-Oxygen Vacancy Pair in $SrTiO_3$ by Paramagnetic Resonance. *Phys. Rev.* **1969**, *186* (2), 361–371. https://doi.org/10.1103/PhysRev.186.361.

(70) Botterman, J.; Joos, J. J.; Smet, P. F. Trapping and Detrapping in $SrAl_2O_4$:Eu,Dy Persistent Phosphors: Influence of Excitation Wavelength and Temperature. *Phys. Rev. B* **2014**, *90* (8), 085147. https://doi.org/10.1103/PhysRevB.90.085147.

(71) Tydtgat, C.; Meert, K. W.; Poelman, D.; Smet, P. F. Optically Stimulated Detrapping during Charging of Persistent Phosphors. *Opt. Mater. Express* **2016**, *6* (3), 844. https://doi.org/10.1364/OME.6.000844.

(72) Nakamura, T.; Matsuzawa, T.; Rowlands, C. C.; Beltrán-López, V.; Smith, G. M.; Riedi, P. C. EPR Investigations on Europium(II)-Doped Aluminates. *Faraday Trans.* **1998**, *94* (19), 3009–3012. https://doi.org/10.1039/a804494e.

(73) Hölsä, J.; Aitasalo, T.; Jungner, H.; Lastusaari, M.; Niittykoski, J.; Spano, G. Role of Defect States in Persistent Luminescence Materials. *Journal of Alloys and Compounds* **2004**, *374* (1–2), 56–59. https://doi.org/10.1016/j.jallcom.2003.11.064.

(74) Nag, A.; Kutty, T. R. N. The Light Induced Valence Change of Europium in Sr_2SiO_4:Eu Involving Transient Crystal Structure. *J. Mater. Chem.* **2004**, *14* (10), 1598-1604. https://doi.org/10.1039/b400515e.

(75) Nag, A.; Kutty, T. R. N. The Mechanism of Long Phosphorescence of $SrAl_{2-x}B_xO_4$ ($0<x<0.2$) and $Sr_4Al_{14-x}B_xO_{25}$ ($0.1<x<0.4$) Co-Doped with Eu^{2+} and Dy^{3+}. *Mater. Res. Bull.* **2004**, *39* (3), 331–342. https://doi.org/10.1016/j.materresbull.2003.11.007.

(76) Wertz, J. E.; Bolton, J. R. *Electron Spin Resonance: Elementary Theory and Practical Applications*, Chapman&Hall.; New York, **1986**.

(77) Wu, S.-Y.; Lin, J.-Z.; Fu, Q.; Zhang, H.-M. Investigations on the Impurity Displacements and the *g* Factors of the Two Tetragonal Ni^{3+} Centres in $SrTiO_3$. *Phys. Scr.* **2007**, *75* (2), 147–151. https://doi.org/10.1088/0031-8949/75/2/005.

(78) Schoenberg, A.; Suss, J. T.; Luz, Z.; Low, W. Dynamic Jahn-Teller Effect in the EPR Spectrum of Ni^{1+} and Ni^{3+} in Magnesium Oxide. *Phys. Rev. B* **1974**, *9* (5), 2047–2050. https://doi.org/10.1103/PhysRevB.9.2047.

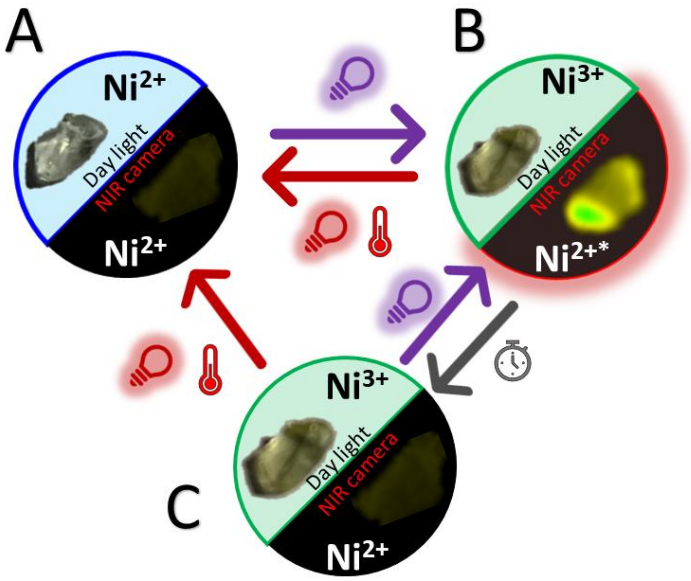

Table of Contents Graphic.